Sensors & Transducers, Vol. 258, Issue 4, July 2022, pp. 10-17

www.sensorsportal.com

Sensors & Transducers

Published by IFSA Publishing, S. L., 2022
http://www.sensorsportal.com

Terahertz Optoelectronic Devices Based on Three-Dimensional Modelling of Symmetrically Coupled Surface Plasmon Polariton Resonances in Bulk Dirac Semimetal

[1] Tony Mathew Blessan, [2] M. Gayathri, [2] T. Alagesan, [1, 3*] N. Yogesh

[1] Department of Nuclear Physics, University of Madras (Guindy Campus), Chennai -600025, India
[2] Department of Physics, Presidency College, Chennai 600005, India
[3] Department of Physics, National Institute of Technology (Calicut), Kerala -673601, India
E-mail: yogesh@nitc.ac.in

Received: 20 June 2022 /Accepted: 22 July 2022 /Published: 29 July 2022

Abstract: Bulk Dirac Semimetal (BDS) - a three-dimensional counterpart of graphene, prominently known for its topologically protected linear dispersion energy bands embraces remarkable plasmonic responses at terahertz (THz) frequencies, which can be well capitalized for its optoelectronic applications. Recently, we have demonstrated the BDS based THz plasmonic applications such as surface plasmon polariton assisted microparticle sensing, THz waveguiding with curved/bending geometries and all-optical THz logic gates. However, all of the demonstrations were restricted with 2-D BDS geometries where height of the BDS was assumed to be infinity. For practical applications, it is essential to consider the height dimension in device realization. In this work, we demonstrate 3-D numerical modelling results of BDS based THz applications by considering height dimension of the BDS in the design of curved waveguides, sub-wavelength waveguiding in tapered geometries and 3-D XOR logic gate. We anticipate that the above findings manifest BDS as a potential candidate for opening new avenues in the realization of THz optoelectronic devices.

Keywords: Bulk Dirac semimetal (BDS), Sub-wavelength waveguiding, THz logic gate, 3-Dimensional, Surface plasmon polariton (SPP).

1. Introduction

Photonic circuits having high operating speed faces the challenge of critical low dimension sizes whereas electronic circuits in nanometer scales have very low operating speed. Therefore, achieving a circuitry device with sub-diffraction dimension and high operational speed is of prime importance. Hence, an optoelectronic integrated circuit that provides enhanced operational speed, low power consumption and reduced interconnect delay in optical communications is highly warranted [1]. One of the key technologies to realize optoelectronic integrated circuit in 3-D geometries is plasmonics [2]. Surface Plasmon Polariton (SPP) are the quanta of quasi-interaction between electromagnetic (e-m) wave and plasmons (collective excitations of electrons) at the interface between plasmonic material and a dielectric [3]. This light-matter interaction is best suited for miniaturized photonic circuits due to its sub-wavelength features [4, 5]. At optical frequencies, bulk metals show negative dielectric permittivity and they exhibit plasmonic response [6]. However, extending conventional metals such as Au, Ag and Cu to excite SPP in THz regime is a cumbersome task as Lorentz-Drude model predicts a high value of

imaginary dielectric permittivity ($\varepsilon_r^{"}$) [7]. The availability of natural materials with plasmonic response is also limited in the THz range (0.1 THz -10 THz). It is to be mentioned that various different techniques such as periodic metal gratings [8] and artificial materials like metamaterials, graphene [9] are also employed for THz plasmonic applications.

In the past few years, relativistic fermions were found to be emerged as low-energy excitations in materials known as Dirac semimetals [10]. Therefore, researchers are exploring the option of employing bulk Dirac semimetals (BDS) such as Cd_3As_2 [11], Na_3Bi and $ZrTe_5$ for SPP interaction in the THz regime. In a typical BDS, electronic states are extended in all three dimensions and therefore one can expect 3-D Dirac points (point at which valence and conduction bands meets) instead of 1-D Dirac points as in the case of graphene. Due to 3-D extension of dispersion in BDS, carrier mobility in BDS is very high [12–15] and this unique bandstructure constitutes BDS as a suitable material for optoelectronic applications at THz waveband [16-19].

In our previous study, we have reported how the curved geometries of BDS sustain THz SPPs using Kretschmann–Raether and Otto configurations [20]. Moreover, in our latest report we also demonstrated the possibility of SPP waveguiding and all optical THz logical gates with BDS [21]. However, BDS were treated as 2-D geometries, in which height of the BDS was taken to be infinity. For practical consideration, one needs to take care of the height dimensions. In this work, we have performed 3-D numerical simulation with BDS for THz waveguiding in straight and curved geometries so that reliability of the results is not only validated, but also, we have attained a step towards device prototypes for novel THz optoelectronic applications. By exciting symmetrically coupled SPP in multilayer BDS, two different 3-D tapered geometries for sub-wavelength waveguiding are demonstrated in this work. Furthermore, a simple Y structured geometry for the functioning of THz plasmonic gate (XOR) is illustrated with the idea of integrating BDS with photonic circuits.

2. Bulk Dirac Semimetal

The Dirac semimetal is an unusual material in which the nodes of the bulk electronic states are protected against the gap formation by crystalline symmetry leading to high carrier mobility and dramatically reduced intrinsic Ohmic losses. We observe that BDS is a promising candidate for THz plasmonic applications in the regime (0.5 THz – 2 THz) by theoretically analyzing its dielectric response. The dielectric response of a BDS is expressed as $\varepsilon_r(\omega) = \varepsilon_\infty + \frac{i\sigma(\omega)}{\omega\varepsilon_0}$ where $\varepsilon_\infty = 13$, ε_0 is the permittivity of vacuum and conductivity $\sigma(\omega)$ is obtained from Kubo formalism as

$$\sigma(\omega) = \frac{ie^2}{\hbar}\frac{g_1}{6\pi^2 v_F \hbar^2}\frac{\mu_c^2 + \frac{(k_B T)^2}{3}}{(\omega + i\tau^{-1})}$$ where $T = 300$ K is the temperature, $\tau = 1.2$ ps is the relaxation time, k_B is the Boltzmann constant, $v_F = 0.9\times10^6\, ms^{-1}$ is the Fermi velocity, $g_1 = 4$ is the degeneracy factor and $\mu_c = 0.1\, eV$ is the chemical potential [22]. At lower THz regime, intraband conductivity dominates and thus contribute to the SPP formation, and hence the interband conductivity has not been taken into account in $\sigma(\omega)$ equation mentioned above.

One striking advantage of BDS is its tunability and it is usually achieved by varying the Fermi energy that can in turn alter the dielectric permittivity of BDS. To what extent the Fermi energy can be varied at room temperature (such that linear dispersion of energy band still holds) is a question of experimental analysis. However, under low temperature and long wavelength limit, theoretically the E_F can be varied from 0.03 eV – 0.15 eV in order to maintain the linear dispersion regime. Additionally, it is noteworthy to mention that relaxation time of charge carriers in BDS also plays an important role in the dielectric permittivity of BDS. Fig. 1(a) shows the dielectric permittivity of BDS at $E_F = 0.1$ eV for above mentioned parameters. Fig. 1(b) is plotted for three varying E_F as 0.06 eV, 0.10 eV and 0.14 eV. Fig. 1(c) emphasizes how the relaxation time influences the dielectric permittivity of BDS when $\tau_s = 0.157$ ps (experimental reference [23]) and $\tau_s = 1.2$ ps. One can infer from Fig. 1(a) that BDS is an excellent candidate for supporting SPP in 0.1 THz – 2 THz regime because the imaginary part of ε_r is considerably small. To comprehend it, as an example one can witness from Table 1 and 2 how Fermi energy and relaxation time manifest dielectric response of BDS at f = 0.9 THz. This frequency is chosen for demonstrative purposes. However, one can chose any value from 0.1 – 2 THz.

All the numerical simulations performed in this work are performed at $E_f = 0.1$ eV and $\tau_s = 1.2$ ps.

Table 1. E_f vs ε_r at f = 0.9 THz and τ_s = 1.2 ps.

Fermi Energy E_f (eV)	ε_r '	ε_r ''
0.06	- 555.2	81.83
0.10	- 1485	218.8
0.14	- 2880	424.3

Table 2. τ_s vs ε_r at f = 0.9 THz and E_f = 0.1eV.

Relaxation Time τ_s (ps)	ε_r '	ε_r ''
0.157 [23]	-657.9	755.7
1.2	-1477	219.6

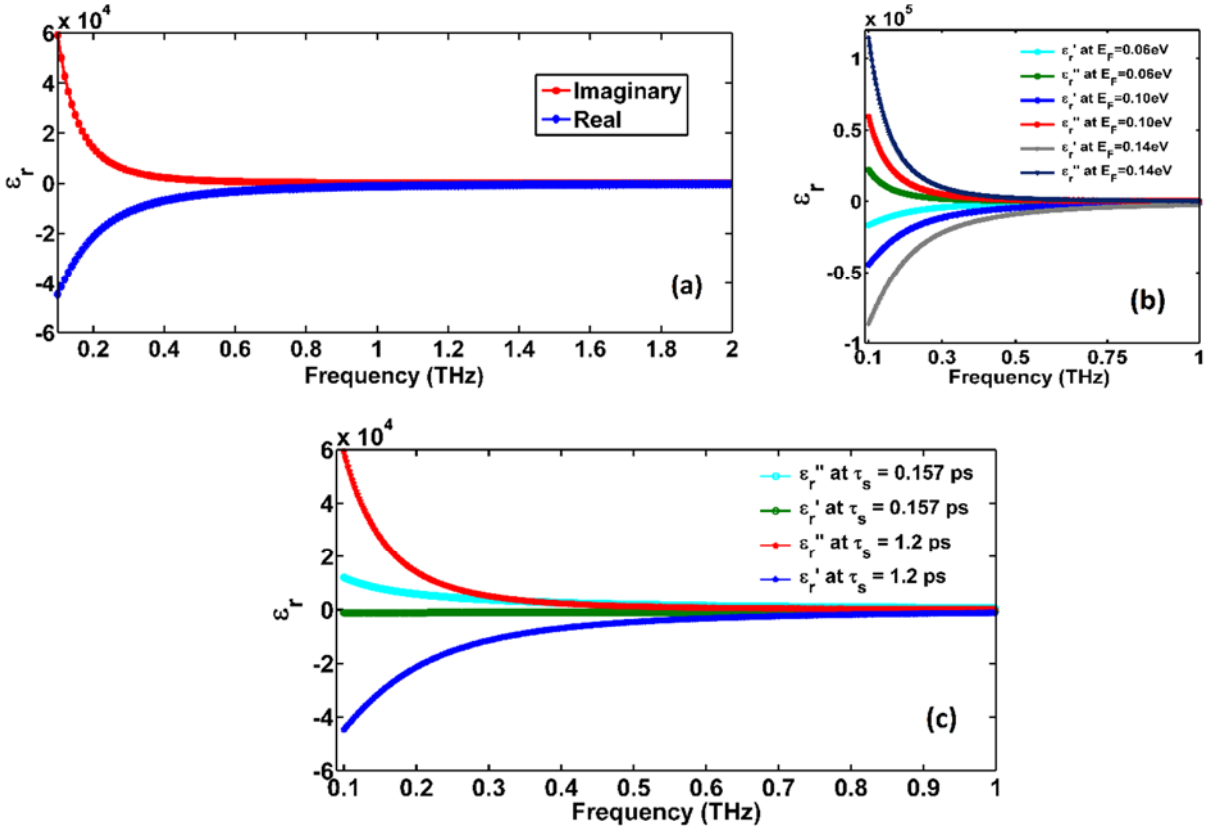

Fig. 1. a) Dielectric permittivity of BDS at E_f = 0.1 eV and τ_s = 1.2 ps; b) varying E_f at τ_s = 1.2 ps; c) varying τ_s at E_f = 0.1 eV.

3. THz SPP Waveguiding in 3-D Curved BDS Geometry

One of the main limitations in guiding geometries are the radiation leakages along sharp bends and corners. Here we demonstrate how SPP in BDS can overcome the issue of losses along corners and bends. It is known that when the separation between two adjacent BDS sheets is smaller than the skin depth, SPP at each BDS boundaries can interact together to form a coupled propagating (symmetric or anti-symmetric) SPP mode. In our previous work [20, 21], detailed analysis of THz SPP sustainment in single and multilayer BDS curved geometries have been examined. In order to deduce whether anti-symmetric or symmetric mode SPP is most suitable for long range waveguiding, eigen mode analysis were performed in single and multilayer BDS geometries. It was found that the real part of the wave vector ($\mathrm{Re}(\beta)$) of the symmetric mode is higher than anti-symmetric mode and this concluded why symmetrically coupled THz SPP mode are preferred over anti-symmetric SPP mode [21]. Here we extent our analysis to 3-D BDS geometries. Firstly, BDS-Air-BDS multilayer with optimized air gap ($\boldsymbol{g}$) of 50 µm between two BDS slabs of height 850 µm and optimized thickness of 7 µm (shown in Fig. 2(a)) is modelled with scattering boundary conditions in all three directions and solved using COMSOL RF module [24] with boundary mode analysis. The choice of BDS height after optimization is taken as 850 µm with the aim that there is minimum amount of transmission losses. Using industrial chemical vapor deposition technique and 3-D laser printing one can coat BDS over a large area substrate and therefore the choice of 850 µm height for BDS sheet may be possible to realize in near future. The H_z field profile at 1.9 THz given in Fig. 2(b) shows the sustainment of SPP mode in BDS parallel waveguide. When a perturbation is introduced in the form of a macrobend (radius of curvature is 500 µm) as shown in Fig. 2(c), SPP still sustained along the bend. At f =1.9 THz, the S_{21} for straight and curved BDS is 93.67 % and 91.32 % respectively. For a curved geometry with radius of curvature 500 µm, the transmission loss is negligible (~0.0235 %) when compared to straight geometry and the corresponding H_z field profile at 1.9 THz given in Fig. 2(d) ascertains that symmetric SPP can evade bends efficiently without much losses, as SPP is confined within the BDS walls.

4. Sub-wavelength THz SPP Waveguiding

The control of electromagnetic wave at sub-wavelength scale for channeling light in fibre-optics

and surface-wave waveguides are of great interest among researchers [25]. Our earlier work analysed how tapered geometries in 2-D support symmetrically coupled SPP mode within BDS walls where aperture miniaturization of $\sim\frac{\lambda}{6}$ were achieved [21]. Here we extend the 2-D geometry in order to understand the cut off dimension for the tapered geometry in which the coupling from high aperture to low aperture is controlled by gradually reducing the separation gap (***g***) between the BDS film. Fig. 3(a) shows a parallel BDS waveguide with dimensions $50\ \mu m \times 300\ \mu m$ tapered to a width of $80\ \mu m$ on both input and output. The corresponding transmission plot in Fig. 3(b) shows that the THz beam propagation is allowed in tapered geometry with above 83% transmission efficiency for the range of 0.85 THz - 2 THz. The inset in Fig. 3(b) shows the H_z field map at f = 1 THz exhibiting sub-wavelength behavior. However, when the dimension of BDS waveguide is reduced to $1\ \mu m \times 300\ \mu m$ with the tapering geometry dimension of $80\ \mu m$ as shown in Fig. 3(c), all frequencies from 0.85 THz – 2 THz are completely forbidden which is evident from the S_{21} plot (Fig. 3(d)) and H_z field map at f = 1 THz (inset of Fig. 3(d)). This indicates that the tapered geometry has a cut off at $\boldsymbol{g} = 1\ \mu m$. It is noteworthy to mention here that the cut off characteristics has been studied with 2-D BDS geometries. Because retrieving S_{21} parameter for a large range of frequencies is cumbersome for 3-D case. Nevertheless, we try to solve field map for a particular frequency proficiently in 3-D geometry by choosing a single frequency from the S_{21} plot of 2-D geometry. Two different tapered 3-D geometries are modelled for studying the sub-wavelength guiding of BDS waveguide. In Fig. 4(a), an air-filled perfect magnetic conducting (PMC, $\hat{n} \times \vec{H} = \vec{0}$) waveguide of dimension $300\ \mu m \times 50\ \mu m \times 850\ \mu m$ is connected with two tapered geometries with dimension of $350\ \mu m \times 80\ \mu m \times 850\ \mu m$ at both input and output interfaces. As a support, SiO_2 substrate ($\varepsilon_r = 4.2$) of dimension $1020\ \mu m \times 600\ \mu m \times 50\ \mu m$ is placed at the bottom. In Fig. 4(b), H_z field pattern at 1 THz shows that PMC tapered waveguide does not allow beam to pass through it. However, in case of parallel BDS waveguide of same dimensions shown in Fig. 5(a), THz beam propagation is allowed with 96 % transmission at f = 1 THz. The field pattern given in Fig. 5(b) at 1 THz reveals sub-wavelength guiding behaviour of multilayer BDS system.

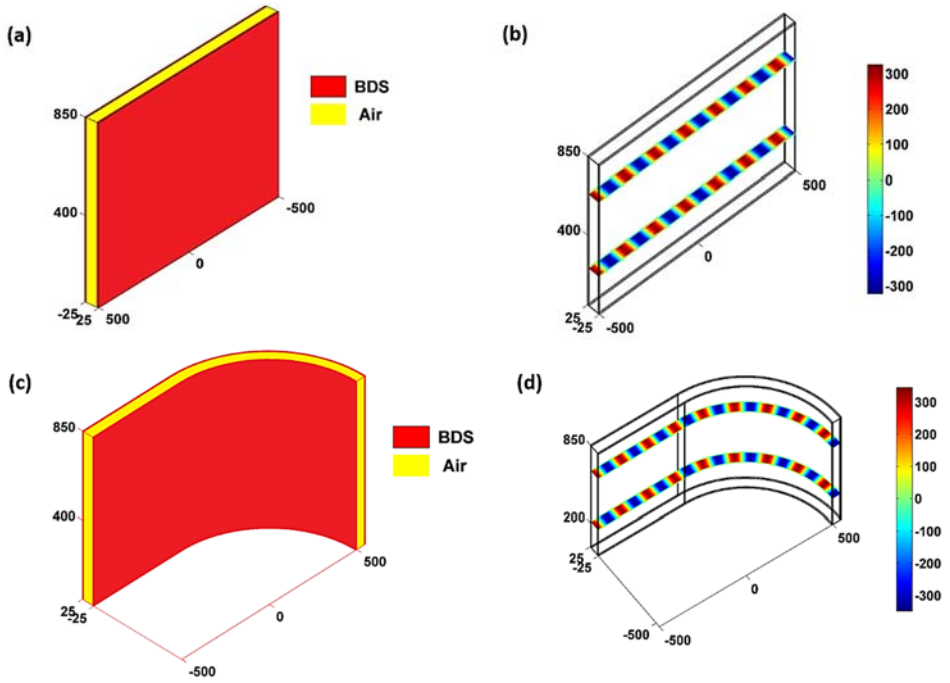

Fig. 2. BDS-Air-BDS configuration a) Straight 3-D geometry; b) H_z field map at 1.9 THz in straight geometry; c) Macro bend 3-D geometry; d) H_z field map at 1.9 THz in macro bend 3-D geometry.

Apart from tapered geometry, we have also tested whether any shape of BDS waveguide sustains SPP confinement. For this purpose, an arch of radius 500 μm and 50 μm × 850 μm dimension is designed with two tapered geometries with dimension 437 μm × 80 μm × 850 μm at both input and output interfaces as shown in Fig. 6(a). To support the configuration, SiO_2 substrate ($\varepsilon_r = 4.2$) of dimension $2010\ \mu m \times 700\ \mu m \times 50\ \mu m$ is placed at the bottom. In order to see the response of arch geometry, initially S_{21} plot is obtained for 2-D geometry. As the arch geometry is a semicircle of resonating nature, one expects periodic dip in S_{21} plot and it is evident from

Fig. 5(b). From S_{21}, two frequencies are chosen such that one frequency is allowed and other is prohibited and these two specific frequencies are solved in 3-D geometry. H_z field pattern in Fig. 5(c) corresponds to f = 0.948 THz in which maximum transmission efficiency of more than 85 % is observed and in Fig. 5(d) H_z profile at 1.152 THz is given, where transmission efficiency is observed to be less than 48%. Hence, from the above results it is clear that coupled SPP modes can be guided for any tapered geometry with good efficiency for larger bandwidth.

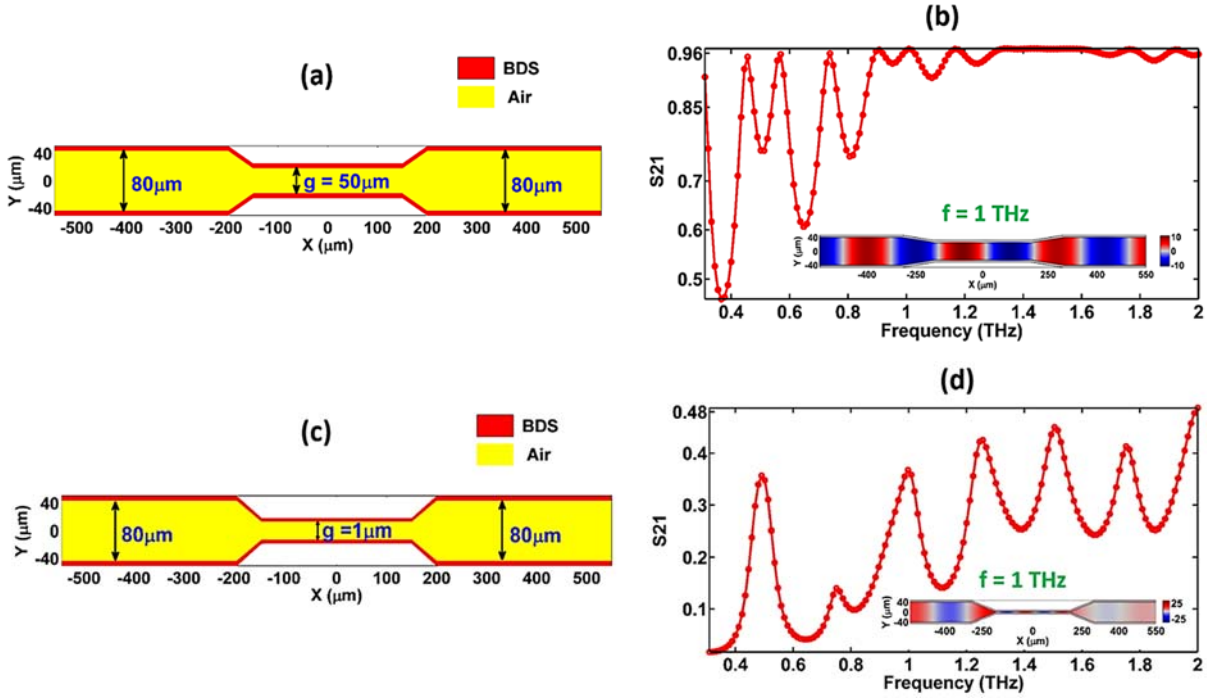

Fig. 3. (a) 2-D geometry of tapered multilayered BDS waveguide of 50 μm; (b) corresponding transmission plot and H_z field at 1 THz shown in the inset; (c) 2-D geometry of tapered multilayered BDS waveguide of 1μm; (d) corresponding transmission plot and H_z field at 1 THz is shown in the inset.

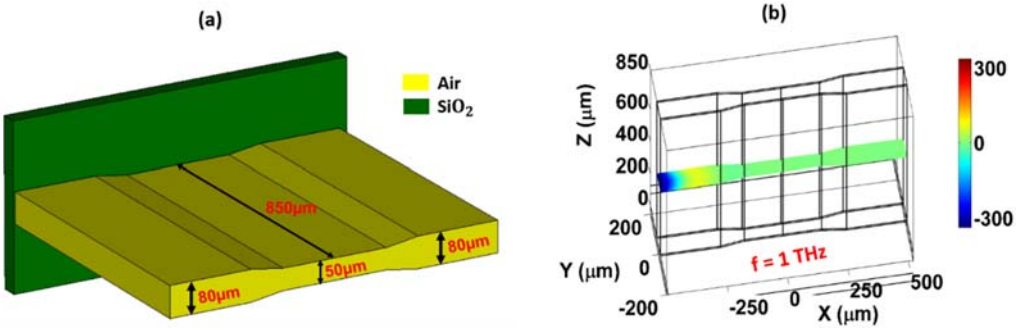

Fig. 4. (a) 3-D geometry of air filled PMC waveguide; (b) H_z field map of 3-D geometry at 1 THz.

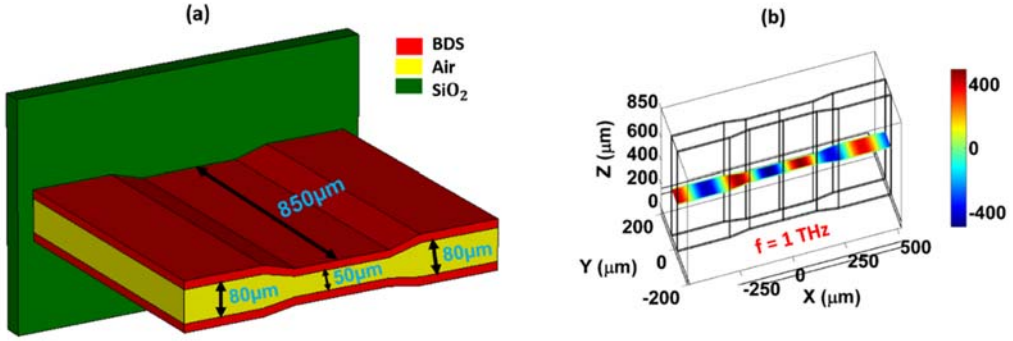

Fig. 5. (a) 3-D geometry of multilayer BDS waveguide; (b) H_z field map of 3-D geometry at 1 THz.

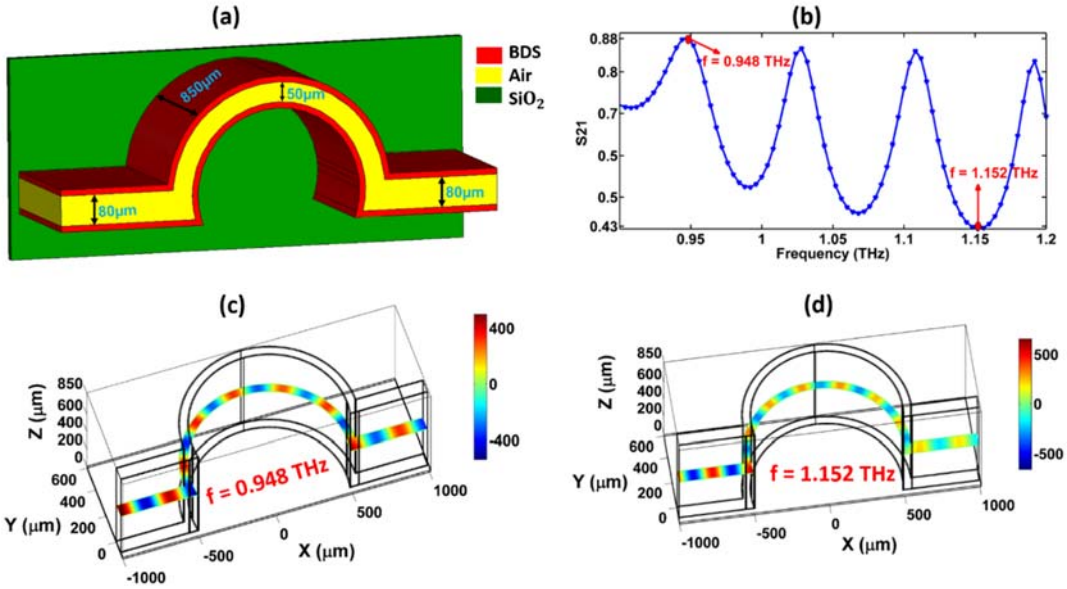

Fig. 6. (a) 3-D geometry of multilayered BDS arch waveguide; (b) transmission plot obtained from 2-D arch geometry, and (c) and (d) H_z field map at 0.948 and 1.152 THz for 3-D arch geometry.

5. Plasmonic Terahertz Logic Gates

Logic gates have potential applications especially in the field of information processing because of its high speed performance with minimum power consumption. They serve as basic components of an optical signal processing system and act as a bridge between electrical and optical calculations [26]. Various research groups have achieved logic gates using metamaterials [27] and photonic crystals [28]. One notable contribution was in developing sub-wavelength graphene-based plasmonic 3-D waveguide that performs THz AND/OR logic gate [29]. In this section, the waveguiding feature (Fig. 2) shown already in parallel BDS system with circuit miniaturization can be extended to the realization of logic gates as it is an essential component for the empowerment of THz optoelectronics. Considering the evading nature of symmetric mode SPP in macro bend geometry, one can very well reach out its application to logic gate. Fig. 7(a) shows the geometry of XOR gate in the form of Y-structure whose input arms are separated by 136 μm and the continuing arm of length 600 μm serves as an output. When symmetric coupled SPP modes in each input arm are in phase with each other, constructive interference occurs and when they are 180˚ out of phase with each other, destructive interference takes place which cancels out the output signal in the detection port. To support the Y configuration, SiO_2 substrate ($\varepsilon_r = 4.2$) of dimension 1500 μm × 600 μm × 50 μm is placed at the bottom. The norm of magnetic field strength ($|\vec{H}|$) patterns shown in Fig. 4(b), 4(c) and 4(d) demonstrate XOR gate at frequency 1.192 THz. The output transmission level less than 50 % can be marked as a threshold for OFF state. Interestingly, the destructive interference of coupled SPP modes corresponds to low transmission level of 15.60 % at 1.192 THz. Table 3 shows the truth table for XOR gate at 1.192 THz.

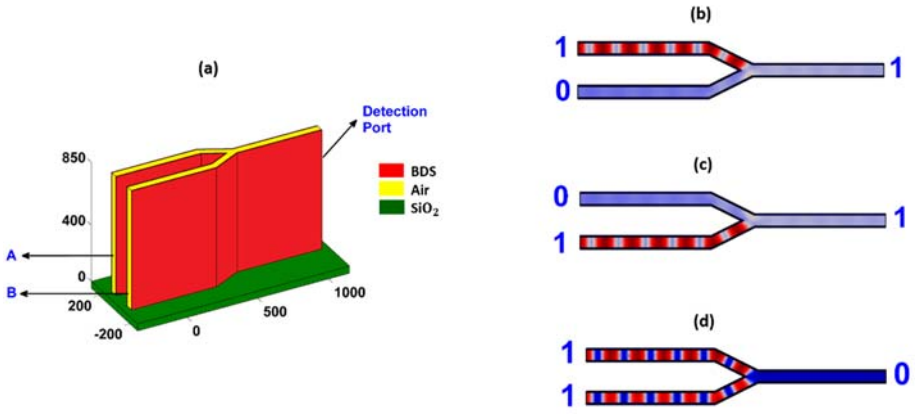

Fig. 7. (a) 3-D logic gate design formed by parallel BDS structure; (b) - (d) represent norm of $\vec{H}$ field patterns for XOR gate at 1.192 THz.

Table 3. Truth table for XOR gate.

Input		Output (S21%)
A	**B**	**XOR (1.192 THz)**
0	0	0
1	0	62.90
0	1	62.91
1	1	15.60

6. Conclusions

To conclude, 3-D modelling of BDS multilayer system in straight and bending geometries were studied. By exploiting coupled SPP modes, subwavelength THz waveguiding in two different tapered geometries were illustrated. A 3D THz XOR logic gate has been successfully demonstrated by utilizing the interference nature of SPP. The above reported 3D waveguide, logic gate and along with the advent of operating room temperature BDS [24, 30], we believe that designing BDS based THz optoelectronics devices will open new horizon on chip scale circuitry levels.

Acknowledgements

This work was done based on the facilities funded by the Department of Science and Technology, Ministry of Science and Technology, India (DST/INSPIRE/04/ 2015/002420).

References

[1]. Liu Y., Zhang J, Peng L. M., Three-dimensional integration of plasmonics and nanoelectronics, *Nat Electron*, Vol. 1, 2018, pp. 644-651.

[2]. Mallikarjun G. Hudedmani, Bindu Suresh Pagad, Plasmonics: A. Path to Replace Electronics and Photonics by Scalable Ultra-fast Technology, *Advanced Journal of Graduate Research*, Vol. 7, Issue 1, 2020, pp. 37-44.

[3]. J. R. Sambles, G. W. Bradbery, and F. Z. Yang, Optical excitation of surface plasmons: An introduction, *Contemp. Phys.,* Vol. 32, Issue 3, 1991, pp. 173-183.

[4]. D. K. Gramotnev and S. I. Bozhevolnyi, Plasmonics beyond the diffraction limit, *Nat. Photonics*, Vol. 4, 2010, pp. 83–91.

[5]. W. L. Barnes, A. Dereux, and T. W. Ebbesen, Surface plasmon subwavelength optics, *Nature*, Vol. 424, 2003, pp. 824–830.

[6]. K. Takagi, S. V. Nair, R. Watanabe, K. Seto, T. Kobayashi, E. Tokunaga, Surface plasmon polariton resonance of gold, silver, and copper studied in the kretschmann geometry: dependence on wavelength, angle of incidence, and film thickness, *J. Phys. Soc. Jpn*., Vol. 86, Issue 12, 2017, pp. 1-11.

[7]. Q. Li, Z. Tian, X. Zhang, R. Singh, L. Du, J. Gu, J. Han, W. Zhang, Active graphene–silicon hybrid diode for terahertz waves, *Nat. Commun*., Vol. 6, 2015, pp. 1-6.

[8]. L. Liu, C. Yang, J. Yang, H. Xiang, Dezhuan Han, Spoof surface plasmon polaritons on ultrathin metal strips: from rectangular grooves to split-ring structures, *J. Opt. Soc. Am. B*, Vol. 34, Issue 6, 2017, pp. 1130–1134.

[9]. A. N. Grigorenko, M. Polini, K. S. Novoselov. Graphene plasmonics, *Nat. Photon.,* Vol. 6, 2012, pp. 749–758.

[10]. Tang, P., Zhou, Q., Xu, G., Dirac fermions in an antiferromagnetic semimetal, *Nature Phys.,* Vol. 12, 2016, pp. 1100–1104.

[11]. Z. Wang, H. Weng, Q. Wu, X. Dai and Z. Fang, Three-dimensional Dirac semimetal and quantum transport in Cd_3As_2, *Phys. Rev. B*, Vol. 88, Issue 125427, 2013, pp. 1-6.

[12]. T. Liang, Q. Gibson, M. N. Ali, M. Liu, R. J. Cava, N. P. Ong, Ultrahigh mobility and giant magnetoresistance in the Dirac Semimetal Cd_3As_2, *Nat. Mater*., Vol. 14, 2014, pp. 280–284.

[13]. S. Borisenko, Q. Gibson, D. Evtushinsky, V. Zabolotnyy, B. Büchner, J. R. Cava, Experimental realization of a three-dimensional Dirac semimetal, *Phys. Rev. Lett.,* Vol. 113, Issue 027603, 2014, pp. 1-5.

[14]. Y. Su, Q. Lin, X. Zhai, X. Luo, L. L. Wang, Controlling terahertz surface plasmon polaritons in Dirac Semimetal sheets, *Opt. Mater. Express*, Vol. 8, Issue 4, 2018, pp. 884–892.

[15]. K. J. A. Ooi, Y.S. Ang, Q. Zhai, X. Sun, P. Xing, C. K. Ong, L. K. Ang, D. T. H. Tan, Dirac terahertz plasmonics in two and three dimensions, *Opt. Commun.,* Vol. 462, Issue 125319, 2020, pp. 1-11.

[16]. Zhu, C., Wang, F., Meng, Y. *et al.*, A robust and tunable mid-infrared optical switch enabled by bulk Dirac fermions, *Nat Commun.,* Vol. 8, Issue 14111, 2017, pp. 1-7.

[17]. Xu, H., Guo, C., Zhang, J., Guo, W., Kuo, C.-N., Lue, C. S., Hu, W. D., Wang, L., Chen, G., Politano, A., Chen, X. S., Lu, W., $PtTe_2$-Based Type-II Dirac Semimetal and Its van der Waals Heterostructure for Sensitive Room Temperature Terahertz Photodetection, *Small,* Vol. 15, Issue 1903362, 2019, pp. 1-7.

[18]. Léonard, François *et al*., Strong Photothermoelectric Response and Contact Reactivity of the Dirac Semimetal ZrTe5, *ACS Applied Materials & Interfaces,* Vol. 9, Issue 42, 2017, pp. 37041-37047.

[19]. Duc Anh Nguyen, Dae Young Park, Juchan Lee, Ngoc Thanh Duong, Chulho Park, Duc Hieu Nguyen, Thi Suong Le, Dongseok Suh, Heejun Yang, Mun Seok Jeong, Patterning of type-II Dirac semimetal $PtTe_2$ for optimized interface of tellurene optoelectronic device, *Nano Energy,* Vol. 86, Issue 106049, 2021, pp. 1-10.

[20]. T. M. Blessan and N. Yogesh, Terahertz surface plasmon polariton resonances and microparticle sensing in bulk Dirac semimetal with spatially perturbed geometries, *J. Opt. Soc. Am. B*, Vol. 38, Issue 8, 2021, pp. 2261-2266.

[21]. T. M. Blessan, C. Venkateswaran and N. Yogesh, All- optical terahertz logic gates based on coupled surface plasmon polariton subwavelength waveguiding in bulk Dirac semimetal, *Optik*, Vol. 257, Issue 168795, 2022, pp. 1-9.

[22]. T. Zhao and Z. Wu, Cherenkov terahertz radiation from Dirac Semimetals surface plasmon polaritons excited by an electron beam, *Chinese Phys. B*, Vol. 29, Issue 034101, 2020, pp. 1-10.

[23]. Z. Dai, M. Manjappa, Y. Yang, T. C. W. Tan, B. Qiang, S. Han, L. J. Wong, F. Xiu, W. Liu and R. Singh, High Mobility 3D Dirac Semimetal (Cd_3As_2) for Ultrafast Photoactive Terahertz Photonics, *Adv. Funct. Mater.*, Vol. 31, Issue 2011011, 2021, pp. 1-9.
[24]. http://www.comsol.com
[25]. Hooper, I., Tremain, B., Dockrey, J. *et al,* Massively Sub-wavelength Guiding of Electromagnetic Waves, *Sci Rep.,* Vol. 4, Issue 7495, 2014, pp. 1-5.
[26]. Yuan, Q. Wang, Y. Li, Y. Xu, Q. Xu, X. Zhang, X. Zhang, J. Han, W. Zhang. Terahertz spoof surface plasmonic logic gates, *iScience*, Vol. 23, Issue 101685, 2020, pp. 1-13.
[27]. E. H. Charles, P. R. Buskohl, C. E. Tabor, R. L. Harne, Digital logic gates in soft, conductive mechanical metamaterials, *Nat. Commun.,* Vol. 12, Issue 1633, 2021, pp. 1-8.
[28]. M. V. Sonth, G. Srikanth, P. Agrawal, B. Premalatha. Basic logic gates in two-dimensional photonic crystals for all optical device design, *Int. J. Electron. Telecommun.*, Vol. 67, Issue 2, 2021, pp. 247–261.
[29]. M. Yarahmadi, M. K. Moravvej-Farshi and L. Yousefi, Subwavelength Graphene-Based Plasmonic THz Switches and Logic Gates, *IEEE Transactions on Terahertz Science and Technology*, Vol. 5, Issue 5, 2015, pp. 725-731.
[30]. Xiaomei Yao, Shengxi Zhang, Qiang Sun, Peizong Chen, Xutao Zhang, Libo Zhang, Jian Zhang, Yan Wu, Jin Zou, Pingping Chen, and Lin Wang, Thickness-Controlled Three-Dimensional Dirac Semimetal for Scalable High-Performance Terahertz Optoelectronics, *ACS Photonics*, Vol. 8, Issue 6, 2021, pp. 1689-1697.